

Robustness and uncertainties in global multivariate wind-wave climate projections

Joao Morim^{1,2,3*}, Mark Hemer^{1,2}, Xiaolan L. Wang⁴, Nick Cartwright¹, Claire Trenham^{1,2}, Alvaro Semedo^{5,6}, Ian Young^{1,7}, Lucy Bricheno⁸, Paula Camus^{1,9}, Mercè Casas-Prat^{1,4}, Li Erikson³, Lorenzo Mentaschi^{1,10}, Nobuhito Mori¹¹, Tomoya Shimura¹¹, Ben Timmermans¹², Ole Aarnes¹³, Øyvind Breivik^{13,14}, Arno Behrens¹⁵, Mikhail Dobrynin¹⁶, Melisa Menendez⁹, Joanna Staneva¹⁵, Michael Wehner¹⁷, Judith Wolf⁸, Bahareh Kamranzad¹⁸, Adrean Webb¹¹, Justin Stopa¹⁹ and Fernando Andutta¹

Understanding climate-driven impacts on the multivariate global wind-wave climate is paramount to effective offshore/coastal climate adaptation planning. However, the use of single-method ensembles and variations arising from different methodologies has resulted in unquantified uncertainty amongst existing global wave climate projections. Here, assessing the first coherent, community-driven, multi-method ensemble of global wave climate projections, we demonstrate widespread ocean regions with robust changes in annual mean significant wave height and mean wave period of 5–15% and shifts in mean wave direction of 5–15°, under a high-emission scenario. Approximately 50% of the world's coastline is at risk from wave climate change, with ~40% revealing robust changes in at least two variables. Furthermore, we find that uncertainty in current projections is dominated by climate model-driven uncertainty, and that single-method modelling studies are unable to capture up to ~50% of the total associated uncertainty.

Wind-waves are dominant contributors to coastal sea-level dynamics^{1,2} and shoreline stability^{3–5}, and can be major disruptors of coastal population⁶, marine ecosystems⁷ and offshore/coastal infrastructures. Future changes to the multivariate global wind-wave climate (significant wave height (H_s), mean wave period (T_m) and mean wave direction (θ_m)) result from a combination of meteorologically driven changes in ocean surface wind fields^{6,8} and morphologically driven changes nearshore (combined effects of changes in sea level⁹, tides and reef structures¹⁰ with long-term changes in beach morphology¹¹). These changes might potentially exacerbate^{12,13}, or even exceed in some coastal regions^{1,14–16}, impacts of future projected sea-level rise. The impacts could be further exacerbated when considering directional changes in wave propagation (θ_m), which is a major driver of coastal stability at all time-scales^{5,9,13,17}. Establishing robust projections of global wave characteristics (by identifying and assessing regions with lack of climate signal and/or intermember agreement) (see Methods)¹⁸, and quantifying the uncertainties introduced by the complex modelling processes used for that purpose, is paramount to preventing potentially costly maladaptation^{19,20}. A problem, however, arises from the wide range of wind-wave methodologies used to derive

wave characteristics from surface winds or pressure fields, which increases the poorly understood uncertainty in existing projections^{21–23}. Consequently, the United Nations IPCC Fifth Assessment Report (AR5)²⁴ assigned low confidence to wave projections (with medium confidence for Southern Ocean H_s increase), owing to the limited number of available model simulations and the uncertainty surrounding Global Climate Model (GCM) down-scaled surface winds.

Since then, a new generation of global wind-wave projection studies has been completed by several international modelling groups^{25–34} using atmospheric forcing fields obtained from the Coupled Model Intercomparison Project Phase 5 (CMIP5) GCM simulations. While each of these independent studies has considered aspects of the uncertainty related to their own specific climate-modelling process, they treated the uncertainty space very differently (such as emission scenarios and/or GCMs). Furthermore, no studies have quantified the uncertainty introduced by their own particular wind-wave modelling method (WMM) to develop global wind-wave fields. This uncertainty stems from different configurations of statistical approaches (including transfer functions, training datasets and predictor corrections) and/or dynamical wind-wave

¹School of Built Environment and Engineering, Griffith University, Southport, Queensland, Australia. ²Commonwealth Scientific and Industrial Research Organisation Oceans and Atmosphere, Hobart, Tasmania, Australia. ³US Geological Survey, Pacific Coastal and Marine Science Center, Santa Cruz, CA, USA. ⁴Environment and Climate Change Canada, Climate Research Division, Toronto, Ontario, Canada. ⁵IHE-Delft, Department of Water Science and Engineering, Delft, the Netherlands. ⁶Instituto Dom Luiz, Faculty of Sciences of the University of Lisbon, Lisbon, Portugal. ⁷Department of Infrastructure Engineering, University of Melbourne, Parkville, Victoria, Australia. ⁸National Oceanographic Centre, Liverpool, UK. ⁹Environmental Hydraulics Institute (IHCantabria), Universidad de Cantabria, Santander, Spain. ¹⁰European Commission, Joint Research Centre, Ispra, Italy. ¹¹Disaster Prevention Research Institute, Kyoto University, Kyoto, Japan. ¹²Climate and Ecosystems Science Division, Lawrence Berkeley National Laboratory, Berkeley, CA, USA. ¹³Norwegian Meteorological Institute, Bergen, Norway. ¹⁴Geophysical Institute, University of Bergen, Bergen, Norway. ¹⁵Helmholtz-Zentrum Geesthacht Centre for Materials and Coastal Research, Geesthacht, Germany. ¹⁶Institute of Oceanography, Center for Earth System Research and Sustainability, Universität Hamburg, Hamburg, Germany. ¹⁷Computational Research Division, Lawrence Berkeley National Laboratory, Berkeley, CA, USA. ¹⁸Graduate School of Advanced Integrated Studies in Human Survivability/Hakubi Center for Advanced Research, Kyoto University, Kyoto, Japan. ¹⁹Department of Ocean and Resources Engineering, University of Hawai'i at Mānoa, Honolulu, HI, USA. *e-mail: joao.morimnascimento@griffithuni.edu.au

models (including source-term parameterizations, sea-ice fields and numerical resolution) (Supplementary Table 1).

Consequently, these studies present contrasting projected changes in wind-wave characteristics (in terms of magnitude and/or signal) across the world's oceans²¹. Such limitations may potentially have hampered broad-scale assessments of future coastal risk and vulnerability^{1,22}. These assessments have either used future H_s changes derived from a very limited number of GCM-forced global wind-wave simulations surrounded by low confidence^{35,36}, or have neglected any future wave changes^{37,38} on the basis of the unavailability of robust global data³⁹ and the high uncertainty among existing studies⁴⁰.

Here, we seek to minimize such limitations by performing a unique analysis of a coordinated, multi-method ensemble of future global wave climate scenarios derived from ten independent state-of-the-art studies^{25–34}, which have been undertaken within a pre-designed, community-driven framework^{41,42}. Combined, these studies yield a large ensemble of 148 members of global wave climate projections from which we identify robust, projected, meteorologically driven changes in H_s , T_m and θ_m at the global scale. Furthermore, this multi-method ensemble of wave projections enables us to quantify (and compare) all three dominant sources of uncertainty (emission scenarios, GCMs and WWMs), which has not been previously attempted owing to lack of multi-method ensembles.

Two^{33,34} of the ten contributing studies employ different statistical approaches to derive global wave projections exploiting relationships between GCM-simulated sea-level pressure fields and wave parameters. The remaining contributions^{25–32} use different configurations of dynamical approaches, in which GCM-simulated, high-temporal resolution near-surface winds are used directly to drive a global wind-wave model. Consult Supplementary Information (Section 1.1 and Supplementary Table 1) for details on each contribution and respective acronyms.

All contributing studies^{25–34} have provided assessments of the performance of their GCM-forced wave simulations to represent the historical wave climate on an independent basis. Here, we compare the model-skill of each ensemble member against the most recent, and complete, calibrated dataset of satellite altimeter H_s measurements of H_s (ref. ⁴³). In addition, we compare the model-skill against the well-validated⁴⁴ ERA-Interim⁴⁵ (ERAI) multivariate (H_s , T_m , θ_m) wave reanalysis for the present-day time-slice (1979–2004) as a common reference dataset. Details of the two databases are described in Methods. We present our model-skill comparisons using Taylor diagrams⁴⁶ at both the global and regional scale, providing spatial correlation, normalized standard deviation (NSD) as well as centred-root-mean-square-difference (CRMSD) within a single diagram. To further support our model-skill analysis, we provide global pairwise comparisons maps of the mean and variability biases for a subset with common forcing GCM-WMM (Supplementary Table 3, Section 5).

Overall, both dynamical and statistically based simulations exhibit good agreement relative to satellite measurements and ERAI. CRMSD values in annual/seasonal \bar{H}_s are generally <0.5 m, with NSD values <0.5 m and spatial correlation values >0.9 at global and regional scales, regardless of the reference dataset used here (Supplementary Figs. 1–4, 6–8). The agreement in annual mean 99th percentile significant wave height (H_s^{99}) is relatively similar to that seen for \bar{H}_s . However, we find relatively less model-skill in representing annual H_s^{99} at the regional scale, particularly across the South Atlantic/Pacific and Southern Indian Ocean, with NSD values up to ~ 1 m (Supplementary Fig. 5). The bias values in annual \bar{H}_s and H_s^{99} relative to satellite data are usually below $\sim 10\text{--}15\%$ and $\sim 15\text{--}17.5\%$ over the global ocean, respectively (Supplementary Figs. 12–13). The ensemble mean of each study exhibits biases of less than $\sim 5\%$ in annual \bar{H}_s anywhere, respectively. Comparison against

the ERAI data in terms of annual/seasonal \bar{T}_m and $\bar{\theta}_m$ exhibits good agreement, with CRMSD values <0.5 s and 0.75° , respectively, and spatial correlation values >0.9 (Supplementary Figs. 6–8) at both the global and regional scale (Supplementary Fig. 9). Further discussion on the model-skill at seasonal, regional and interannual scales is provided in Supplementary Information (Sections 3 and 5).

Cluster analysis of \bar{H}_s by member (Methods) over the present-day time-slice delineates groups of ensemble members defined by wave-modelling methodology, rather than by GCM-forcing (Fig. 1). These results, supported by Supplementary Fig. 12, show that WMM strongly dominates the variance in this community ensemble of historical wave simulations (which includes all GCM-forced simulated wave data available to date). Within each WMM cluster, we note close association of members with similar GCM-forcing (that is, GCMs with shared dynamical cores).

Figure 1 shows two well-defined, statistically derived clusters (1 and 5) explained by differences in the training datasets, transfer functions and/or predictor corrections, and three dynamically based clusters (2–4) arising from differences in dynamical wave modelling configurations (for example, model source-term parameterizations). Note that clusters 1 (IHC) and 5 (ECCC(s)) share common characteristics, in which their members have very high similarity as a consequence of their statistical calibrations and predictor corrections^{33,47}. This is also evident in our model-skill comparison (Supplementary Figs. 1–3, 12). Consult Supplementary Information (Section 4) for details on the distinctive qualities of each cluster and for discussion on within-cluster similarities.

Projected future changes in the climatological mean wave fields over the globe by the end of the twenty-first century (2081–2100) are assessed for two representative concentration pathways (RCPs): a medium (RCP4.5) and a high-emission scenario (RCP8.5). RCP4.5 and RCP8.5 exhibit very similar spatial patterns of projected changes for all wave parameters, but the latter shows relatively larger changes (Fig. 2). Signals of projected changes in annual mean wave parameters (\bar{H}_s , \bar{T}_m and $\bar{\theta}_m$) show robust change (Methods) over ~ 36 , 44 and 32% of the global ocean, respectively (under RCP8.5; Supplementary Table 2).

A robust projected decrease in annual \bar{H}_s is seen across the North Atlantic Ocean and portions of the northern Pacific Ocean of up to $\sim 10\%$ under RCP8.5, expanding further across the eastern Indian and southern Atlantic Oceans in austral summer. This is consistent with the relatively uniform decrease in projected surface wind speeds over the boreal extra-tropical storm belt⁴⁸, partially driven by a strongly reduced meridional temperature gradient due to polar amplification of climate change⁴⁹. The areas of robust projected increase are limited to the Southern Ocean and the tropical eastern Pacific—in line with the intensification and poleward shift of the austral westerly storm belt⁵⁰ and increasing Southern Ocean swell propagation into tropical areas²³, respectively. In the austral winter, regions of robust projected increase expand further across the tropics. These findings are overall qualitatively consistent with the Coordinated Ocean Wave Climate Project (COWCLIP) CMIP3 multi-model ensemble²³, and other relevant literature²¹.

Storm significant wave height, H_s^{99} , shows annual/seasonal characteristics of change similar to \bar{H}_s although the fraction of global ocean showing robust changes is much smaller (Fig. 2 and Supplementary Table 2), highlighting the high uncertainty in extreme wave climate projections. Although we present projected changes in extreme H_s^{99} , we draw attention to the ongoing challenge of resolving storm wave conditions generated by intense tropical/extra-tropical storms in wave simulations forced directly with atmospheric surface fields ($\sim 1\text{--}2^\circ$) from CMIP5 GCMs. High-resolution studies^{33,34} have highlighted the importance of increased wind-forcing resolution ($\sim 0.25^\circ$) to adequately capture storm wave climate in tropical cyclone-affected areas, and of the sensitivity of projected changes to resolution.

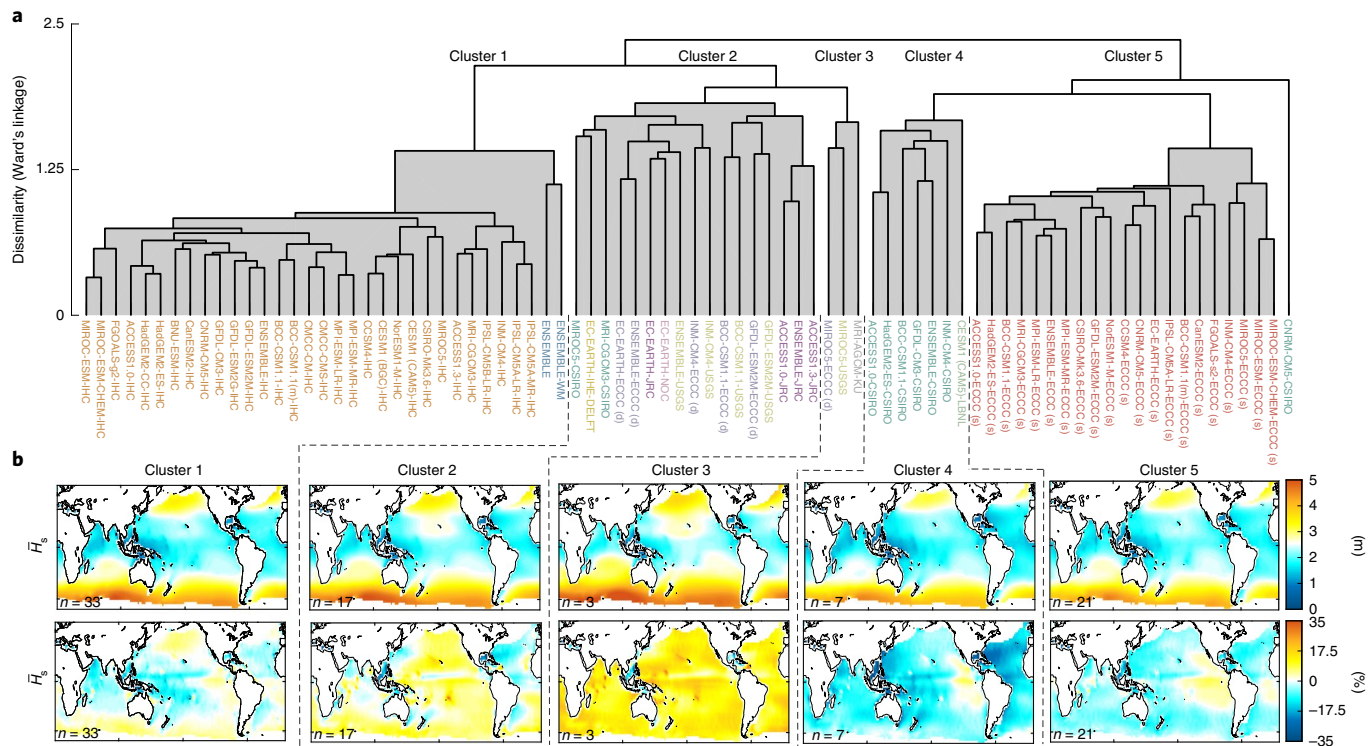


Fig. 1 | Hierarchical clustering of annual \bar{H}_s for the present-day climate (1979–2004). **a**, Cluster tree diagram (dendrogram) resulting from Euclidean distance-based Ward's minimum variance clustering (Methods) using global pairwise annual \bar{H}_s (Methods). The vertical axis represents the distance or dissimilarity between clusters (and cluster members), presented as log-scale for clarity. On the horizontal axis, the members are labelled by GCM and WMM (coloured accordingly). The multi-model ensemble mean from each WMM is also included, with its respective colour. Full multi-member ensemble averages (weighted ensemble mean by WMM, ENSEMBLE-WM and uniformly weighted ensemble mean, ENSEMBLE) are coloured blue (Methods). Grey shading denotes five well-defined key clusters. **b**, Within each dashed line section, maps showing the mean of each cluster in terms of absolute value (top row) and relative percentage difference to the satellite database (bottom row) are shown for annual \bar{H}_s (Methods). The numbers at the bottom left of each panel represent the number of cluster members used to calculate the cluster mean.

The extended influence of the increasing propagation of swells from the Southern Ocean region to the tropics is shown by the robust projected increase in \bar{T}_m (~44% of the global ocean) and the projected shift in $\bar{\theta}_m$ over ~32% of the global ocean (clockwise over the tropical Pacific and tropical Atlantic, anticlockwise elsewhere). Consult Supplementary Figs. 21 and 22 for further discussion on projected future seasonal changes. The results described are mechanistically linked to well-documented, large-scale atmospheric wind circulation changes^{48,49} and modes of natural climate variability²³.

Beyond evaluating the robustness of the projected changes (Fig. 2), we assess the importance of changes relative to the magnitude of present-day interannual variability (see Supplementary Fig. 20). For RCP4.5, and we speculate the same for lower pathways⁵¹, most robust projected changes in wave parameters fall within the range of present natural variability (<100%). Under the high-emission RCP8.5, however, nearly all robust changes exceed the simulated present-day interannual variability (in some regions by >150%).

Figure 3 identifies robust projected changes in offshore multivariate wave conditions (H_s , T_m and θ_m) in the vicinity of the world's coastlines (Methods), which are considered dominant physical drivers of coastal change^{5,6,13,52} and have served as a proxy for broad-scale assessments of coastal risk and vulnerability^{26,35,36,53}. We find that ~50% of the world's coasts (excluding sea-ice areas and enclosed basins) exhibit robust projected changes in the adjacent offshore wave climate in at least one variable (\bar{H}_s , \bar{T}_m or $\bar{\theta}_m$). Whilst there are regions where robust projections are limited to a single variable (for example, $\bar{\theta}_m$ changes off the southern and eastern coasts of Africa), there are several coastal sections (~40% of the

global coastline) where robust changes in offshore \bar{H}_s , \bar{T}_m and/or $\bar{\theta}_m$ coincide (for example, New Zealand, southern Australia and the western coasts of Central and South America). This is also the case for the highly populated North American Atlantic coast (a well-documented hotspot of accelerated sea-level rise⁵⁴, where we find a robust decrease in \bar{H}_s and \bar{T}_m). Future projected changes in $\bar{\theta}_m$ (a key driver of sustained coastal erosion⁵⁵) are robust in the vicinity of 21% of the world's coastlines, with magnitudes ranging $\sim\pm 17^\circ$. We exclude sea-ice-affected regions from our analysis. However, these areas must be acknowledged as future locations of potentially high wave climate change, owing to altered wind and fetch conditions with changing sea-ice extent^{29,56}.

Our community ensemble of global wave climate projections has a range of uncertainty stemming from several different sources (RCPs, GCMs and WMMs) that have remained largely unquantified in previous, stand-alone studies. We applied Ward's analysis of variation (ANOVA)-based clustering (Methods) to a designed subset of projection scenarios (Supplementary Table 3) spanning two RCP emissions scenarios, ten GCM models and eight WMMs, providing an overall analysis of similarity amongst the projected changes (Fig. 4). We find that projected relative changes in \bar{H}_s largely cluster by GCM-forcing (that is, atmospheric forcing from which the wave field originates). There are only a few cases where RCP/WMM-related uncertainties dominate the dissimilarity between projections (for example, MIROC5, BCC-CSM1.1 and CNRM-CM5-forced members). See Supplementary Information (Section 6.3) for further discussion on the distinctive qualities of each cluster.

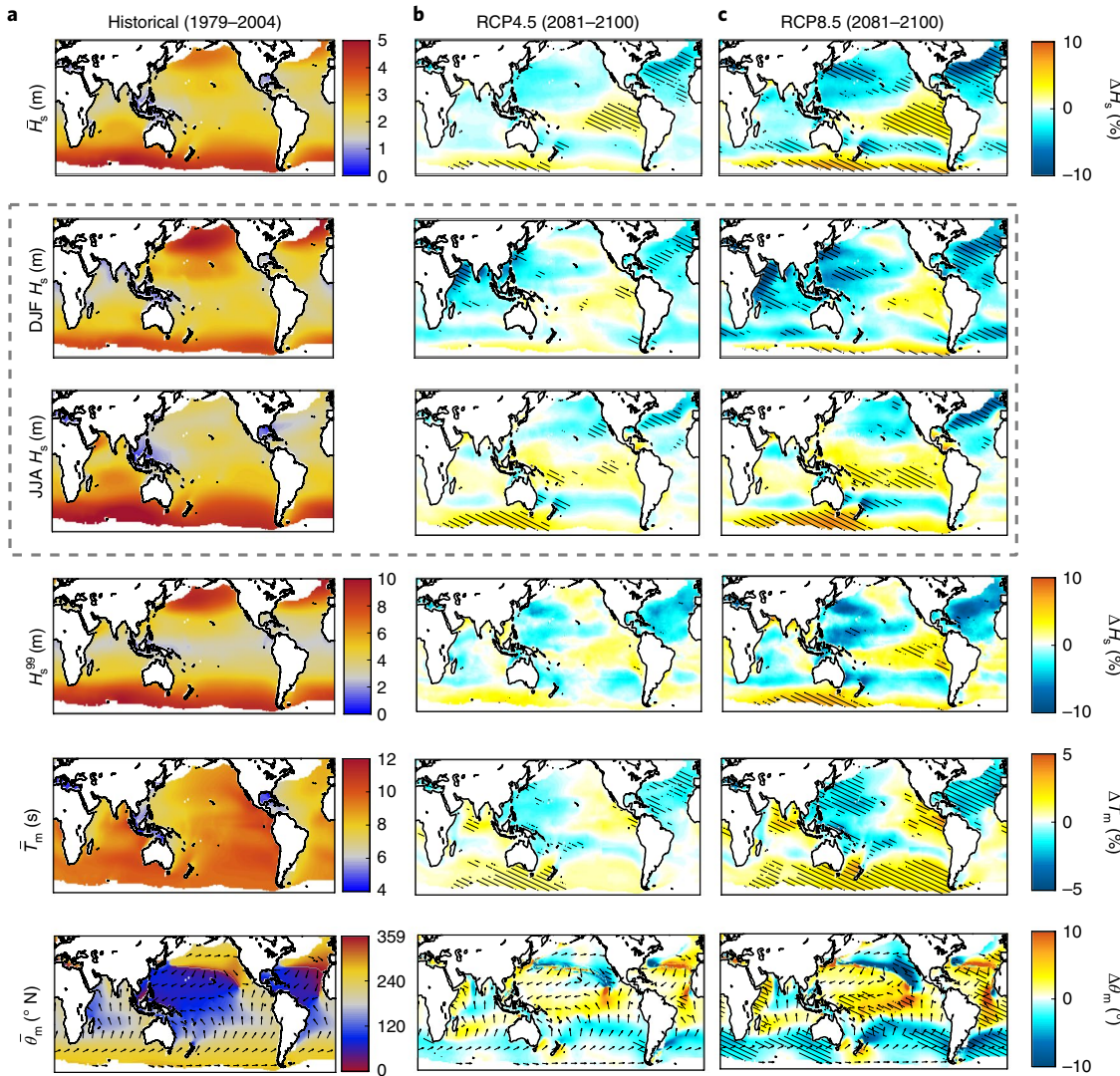


Fig. 2 | Simulated wave climatological mean fields for the present day (1979–2004) and projected changes in climatological wave values for the period 2081–2100 under RCP4.5 and RCP8.5. **a**, Weighted multi-member mean of the 1979–2004 mean of annual mean significant wave height, \bar{H}_s (December–February (DJF) and June–August (JJA)). \bar{H}_s within dashed box with same colour bar as for annual \bar{H}_s ; 99th percentile significant wave height, H_s^{99} ; mean wave period, \bar{T}_m ; mean wave direction, $\bar{\theta}_m$. **b,c**, Weighted multi-member mean of projected changes in the climatological mean of the respective wave parameter for the period 2081–2100 relative to the period 1979–2004 under RCP4.5 (**b**) and RCP8.5 (**c**). Changes are expressed as percentage of present-day climatological values. Changes in $\bar{\theta}_m$ (clockwise) are absolute changes, with vector direction denoting $\bar{\theta}_m$ for the present-day climatological mean field. Hatching indicates areas of robust change (Methods). Seasonal changes for each wave parameter are provided in Supplementary Figs. 21 and 22.

To further quantify the dominant drivers of uncertainty among these global wave climate projections and their relative contribution to the total projection uncertainty, we applied a three-factor, ANOVA-based variance decomposition to three opportunity subsets (Table 4) containing all three sources of uncertainty. See Methods for a description of the selection of the subsets used and the ANOVA methodology. The findings show that no single source of uncertainty is negligible, and that the full projection uncertainty is not solely attributable to the different sources of uncertainty but is also dependent on their interactions. For all subsets available (Fig. 5 and Supplementary Figs. 27 and 28) we find a dominating influence of GCM uncertainty across most of the global ocean, accounting for ~30% to >50% of the total uncertainty associated with projected future changes in climatological mean \bar{H}_s . These results are consistent with our cluster analysis (Fig. 4).

Scenario-driven uncertainty dominates over the North Atlantic, western North Pacific and Southern Ocean (~40% to

>50% full uncertainty), but is exceeded by other uncertainty contributors elsewhere. Choice of WMMs is a significant contributor to full uncertainty, particularly across the tropics/subtropics (~25–50%), and the interactions between uncertainty sources account for ~20–30% of total uncertainty across most of the world's oceans (dominated by GCM–WMM interactions; Fig. 5e). These findings show that all three sources of uncertainty must be adequately sampled to capture the full uncertainty in the projected change signal. They also demonstrate that previous studies relying on a single methodology have not captured up to ~40–50% of total uncertainty space (that is, the sum of all fractions related to WMM).

Our global-scale study does not resolve the uncertainty in projections of wave fields introduced with atmospheric down-scaling techniques. Although the regional down-scaling step has been widely used in wave climate projection studies, and is a topic of intensive research⁵⁷, the various down-scaling techniques introduce an additional source of

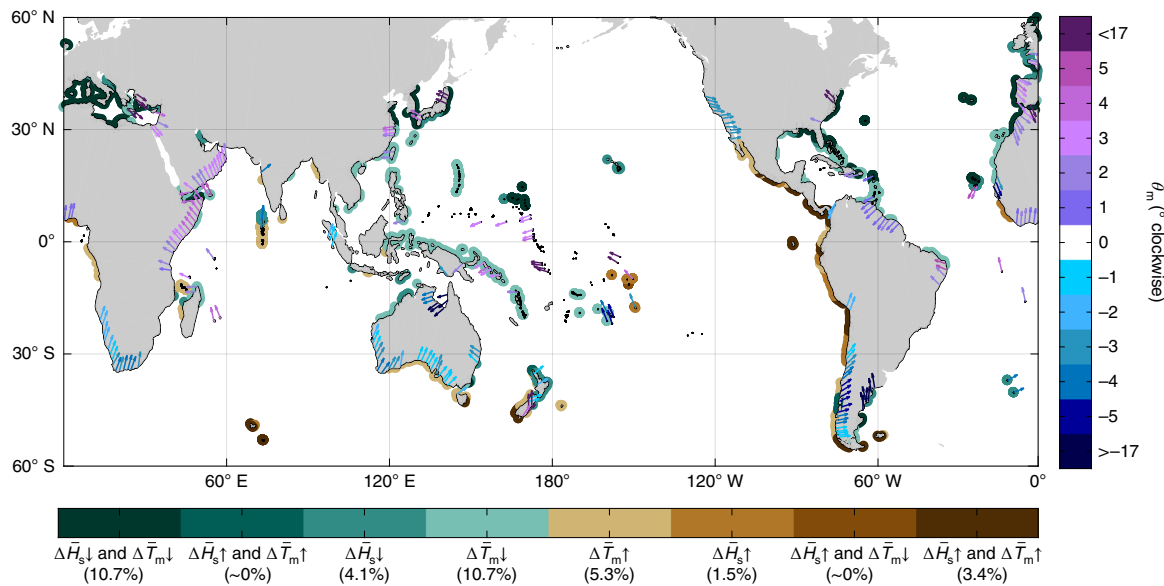


Fig. 3 | Robust projected changes in offshore \bar{H}_s , \bar{T}_m , and $\bar{\theta}_m$ for 2080–2100 (under RCP8.5) in the vicinity of the world's coastlines. Sections exhibiting robust weighted multi-member mean changes under RCP8.5 are coloured according to the qualitative colour bar (bottom), which also shows the percentage of affected coastline where changes are robust (Methods) for each wave characteristic(s). Regions exhibiting a simultaneous robust increase in offshore \bar{H}_s and robust decrease in offshore \bar{T}_m (or vice versa) are extremely limited. Vectors represent robust projected changes in offshore $\bar{\theta}_m$ with their angle degrees north, representing wave direction over the historical time-slice (1979–2004) and their colour representing the magnitude of future changes (according to the quantitative colour bar, right-hand side). The percentage of affected ice-free coastline with robust changes in offshore $\bar{\theta}_m$ is estimated at ~21% (Supplementary Table 2). Coastlines lacking a black outline represent sea-ice areas and enclosed seas, excluded from the analysis (Methods).

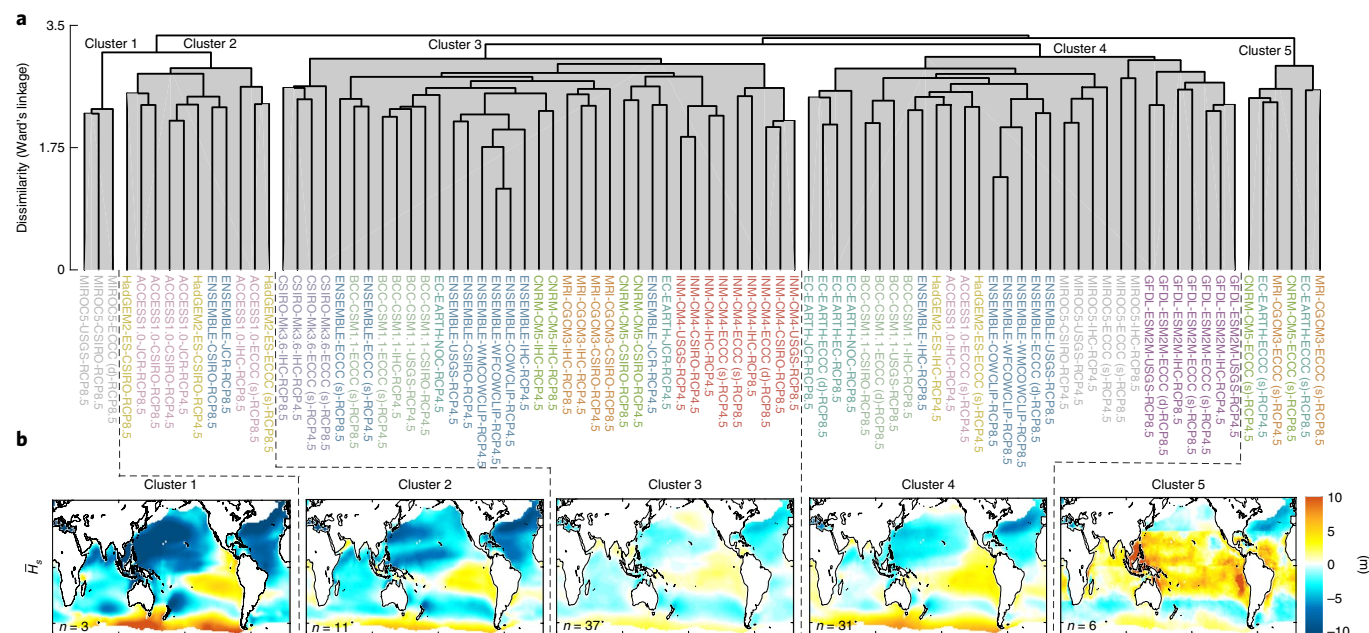


Fig. 4 | Hierarchical clustering of projected relative changes in annual \bar{H}_s (2081–2100 relative to 1979–2004). **a**, Cluster tree diagram resulting from Euclidean distance-based Ward's minimum variance clustering using global pairwise projected annual \bar{H}_s (Methods). The vertical axis represents the distance or dissimilarity between clusters (and cluster members), presented in log-scale for clarity. On the horizontal axis, members are labelled by GCM-forcing, WMM and RCP scenario (RCP4.5 simulations are italicized), respectively, and coloured by GCM, accordingly. The multi-model ensemble mean from each study group is also included. Full multi-member ensemble averages (weighted ensemble mean weighted by WMM, ENSEMBLE-WM, uniformly weighted ensemble mean, ENSEMBLE and ensemble mean weighted by forcing, ENSEMBLE-WF) are coloured blue (Methods). Grey shading denotes five well-defined key clusters. **b**, Within each dashed line section, maps showing the mean of each cluster's projected relative change in annual \bar{H}_s (m) are shown (Methods). The numbers at the bottom left of each panel represent cluster members used to calculate the cluster mean.

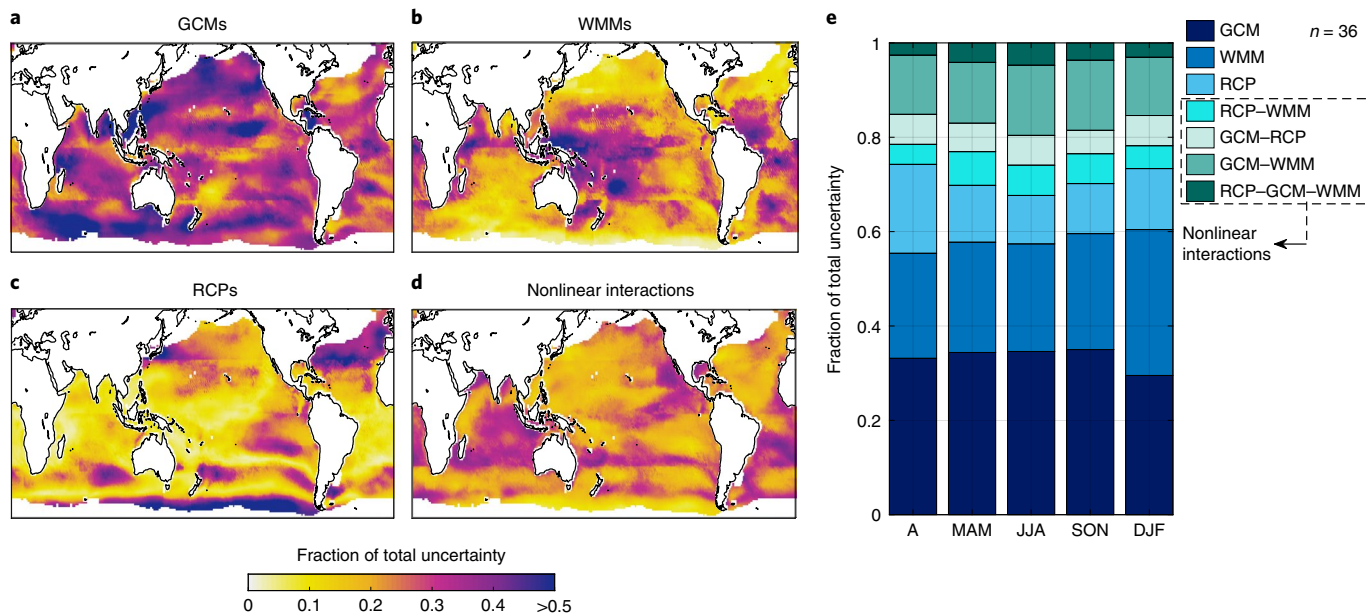


Fig. 5 | Relative contribution of different sources of uncertainty to projected future changes in the mean of annual/seasonal H_s . **a-d,** Fraction of total uncertainty (variance) in projected H_s changes (2081–2100 relative to 1979–2004) attributable to GCMs (**a**), WMMs (**b**) and RCPs (**c**), and sum of all interaction terms (**d**). **e,** Spatially averaged contribution of each uncertainty source and their pairwise and triple interactions with total ensemble uncertainty. A, annual; MAM, March–May; SON, September–November. Results are derived from ensemble subset 2, which consists of six GCMs, two RCPs and three WMMs for a total of $n=36$ simulations (Supplementary Table 4). Similar results are found for subsets 1 and 3, and are presented in Supplementary Figs. 16 and 17. The variance partitioning is based on a three-factor ANOVA model complemented with a subsampling scheme (Methods). Note that plotting artefacts, such as horizontal lines, reflect the effects of the spatial domain partitioning applied in statistical methodologies.

uncertainty that (at present) is not possible to sample at the global-ocean scale.

Our CMIP5-based coordinated ensemble of wave climate projections samples over RCP, GCM and WMMs, thus allowing a much improved sampling of the uncertainty space relative to the COWCLIP CMIP3-based ensemble of opportunity²³, or to any previous study to date²¹. In addition to resolving the largely unquantified contribution of all three dominant sources of uncertainty, this study attests to the importance of considering conceptually distinct wind-wave methodologies. We note that some of the uncertainty seen amongst dynamical simulations in terms of H_s biases could potentially be reduced by further model calibration^{58,59} and improved wind-wave model physics (for example, removal of dependence on spectral model approximations, such as for nonlinear wave-wave interactions⁶⁰ and model limiters for spectral propagation velocities, applied to improve computational efficiency and accuracy^{61,62}). While, at present, it is not possible to isolate these components, we advocate that future dynamical wave studies attempt to reduce the overall H_s historical bias. Regarding model-skill, wind-forcing correction could lead to improved wave model simulations⁵⁹. The results also stress the need for better understanding of the differences in the various global wave reanalyses and hindcasts (used to develop historical trends of wave climate change^{1,63}).

Our results provide a new perspective on the robustness of multivariate global-scale wave projections, building far beyond the restricted range of future wave climate scenarios published in individual studies to date. These coordinated ensemble projections show that signals of wave climate change will not exceed the magnitude of the natural climate variability if the goal of the Paris Agreement target (2 °C) is kept. Under a high-emission scenario (RCP8.5), ~48% of the world's coast is at risk of wave climate change owing to changes in offshore forcing \bar{H}_s , \bar{T}_m and/or $\bar{\theta}_m$ (with ~40% exhibiting robust changes in at least two of these wave variables). The magnitude of future projected changes found for any of these

wave variables (~5–15%) is capable of inducing significant changes in coastal wave-driven processes and their associated hazards⁵².

Broad-scale assessments of coastal impacts of climate change are now beginning to include changes in wave climate^{1,35,36,53}; however, these studies are yet to consider directional shifts in wave propagation, which have been shown to be a dominant driver of shoreline stability^{5,13}. Whilst our results have far-reaching implications from many perspectives, they address only meteorologically driven changes in wind-wave characteristics, which have been the predominant focus of wind-wave climate projection studies to date. Some localized-scale studies suggest that the morphologically driven component of wave climate change might lead to a greater change in coastal zones than these meteorologically driven changes¹¹. Concentrated community effort is now required to quantify morphologically driven wave climate change as a contributor to global coastal water-level changes, as we look towards improved coastal vulnerability assessments from the climate community⁶⁴.

Online content

Any methods, additional references, Nature Research reporting summaries, source data, statements of code and data availability and associated accession codes are available at <https://doi.org/10.1038/s41558-019-0542-5>.

Received: 16 November 2018; Accepted: 2 July 2019;

Published online: 19 August 2019

References

1. Melet, A., Meyssignac, B., Almar, R. & Le Cozannet, G. Under-estimated wave contribution to coastal sea-level rise. *Nat. Clim. Change* **8**, 234–239 (2018).
2. Serafin, A. K., Ruggiero, P. & Stockdon, H. F. The relative contribution of waves, tides, and nontidal residuals to extreme total water levels on U.S. West Coast sandy beaches. *Geophys. Res. Lett.* **44**, 1839–1847 (2017).

3. Harley, M. D. et al. Extreme coastal erosion enhanced by anomalous extratropical storm wave direction. *Sci. Rep.* **7**, 6033 (2017).
4. Barnard, P. L. et al. Extreme oceanographic forcing and coastal response due to the 2015–2016 El Niño. *Nat. Commun.* **8**, 14365 (2017).
5. Barnard, P. L. et al. Coastal vulnerability across the Pacific dominated by El Niño/Southern Oscillation. *Nat. Geosci.* **8**, 801–807 (2015).
6. Hoeke, R. K. et al. Widespread inundation of Pacific islands triggered by distant-source wind-waves. *Glob. Planet. Change* **108**, 128–138 (2013).
7. Feagin, R. A. et al. Does vegetation prevent wave erosion of salt marsh edges? *Proc. Natl Acad. Sci. USA* **106**, 10109–10113 (2009).
8. Young, I. R. & Ribal, Agustinus Multiplatform evaluation of global trends in wind speed and wave height. *Science* **364**, 548–552 (2019).
9. Wandres, M., Pattiaratchi, C. & Hemer, M. A. Projected changes of the southwest Australian wave climate under two atmospheric greenhouse gas concentration pathways. *Ocean Model.* **117**, 70–87 (2017).
10. Albert, S. et al. Interactions between sea-level rise and wave exposure on reef island dynamics in the Solomon Islands. *Environ. Res. Lett.* **11**, 054011 (2016).
11. Oliveira, F. S. B. F. A case study of wave climate changes due to nearshore morphological evolution. *J. Coast. Res.* **24**, 21–32 (2008).
12. Storlazzi, C. D. et al. Most atolls will be uninhabitable by the mid-21st century because of sea-level rise exacerbating wave-driven flooding. *Sci. Adv.* **4**, eaap9741 (2018).
13. Ranasinghe, R. Assessing climate change impacts on open sandy coasts: a review. *Earth Sci. Rev.* **160**, 320–332 (2016).
14. Coelho, C., Silva, R., Veloso-Gomes, F. & Taveira-Pinto, F. Potential effects of climate change on northwest Portuguese coastal zones. *ICES J. Mar. Sci.* **66**, 1497–1507 (2009).
15. Suh, K.-D., Kim, S.-W., Mori, N. & Mase, H. Effect of climate change on performance-based design of caisson breakwaters. *J. Waterw. Port. Coast. Ocean Eng.* **138**, 215–225 (2012).
16. Cowell, P. J., Roy, P. S. & Jones, R. A. Simulation of large-scale coastal change using a morphological behaviour model. *Mar. Geol.* **126**, 45–61 (1995).
17. Hurst, M. D., Rood, D. H., Ellis, M. A., Anderson, R. S. & Dornbusch, U. Recent acceleration in coastal cliff retreat rates on the south coast of Great Britain. *Proc. Natl Acad. Sci. USA* **113**, 13336–13341 (2016).
18. Tebaldi, C., Arblaster, J. M. & Knutti, R. Mapping model agreement on future climate projections. *Geophys. Res. Lett.* **38**, L23701 (2011).
19. Magnan, A. K. et al. Addressing the risk of maladaptation to climate change. *WIREs Clim. Change* **7**, 646–665 (2016).
20. Jones, R. N. et al. in *Climate Change 2014: Impacts, Adaptation, and Vulnerability* (eds Field, C. B. et al.) Ch. 2 (IPCC, Cambridge Univ. Press, 2014).
21. Morim, J., Hemer, M., Cartwright, N., Strauss, D. & Andutta, F. On the concordance of 21st century wind-wave climate projections. *Glob. Planet. Change* **167**, 160–171 (2018).
22. Hemer, M. A., Wang, X. L., Weisse, R. & Swail, V. R. Advancing wind-waves climate science. *Bull. Am. Meteorol. Soc.* **93**, 791–796 (2012).
23. Hemer, M. A., Fan, Y., Mori, N., Semedo, A. & Wang, X. L. Projected changes in wave climate from a multi-model ensemble. *Nat. Clim. Change* **3**, 471–476 (2013).
24. Church, J. A. et al. in *Climate Change 2013: The Physical Science Basis* (eds Stocker, T. F. et al.) 1140–1141 (IPCC, Cambridge Univ. Press, 2013).
25. Hemer, M. A. & Trenham, C. E. Evaluation of a CMIP5 derived dynamical global wind wave climate model ensemble. *Ocean Model.* **103**, 190–203 (2016).
26. Mentaschi, L., Vousdoukas, M. I., Voukouvalas, E., Dosio, A. & Feyen, L. Global changes of extreme coastal wave energy fluxes triggered by intensified teleconnection patterns. *Geophys. Res. Lett.* **44**, 2416–2426 (2017).
27. Erikson, L. H., Hegermiller, C. A., Barnard, P. L., Ruggiero, P. & van Ormondt, M. Projected wave conditions in the Eastern North Pacific under the influence of two CMIP5 climate scenarios. *Ocean Model.* **96**, 171–185 (2015).
28. Bricheno, L. M. & Wolf, J. Future wave conditions of Europe, in response to high-end climate change scenarios. *J. Geophys. Res. Oceans* **123**, 8762–8791 (2018).
29. Casas-Prat, M., Wang, X. L. & Swart, N. CMIP5-based global wave climate projections including the entire Arctic Ocean. *Ocean Model.* **123**, 66–85 (2018).
30. Semedo, A. et al. CMIP5-derived single-forcing, single-model, and single-scenario wind-wave climate ensemble: configuration and performance evaluation. *J. Mar. Sci. Eng.* **6**, 90 (2018).
31. Timmermans, B., Stone, D., Wehner, M. & Krishnan, H. Impact of tropical cyclones on modeled extreme wind-wave climate. *Geophys. Res. Lett.* **44**, 1393–1401 (2017).
32. Tomoya, S., Nobuhito, M. & A., H. M. Variability and future decreases in winter wave heights in the Western North Pacific. *Geophys. Res. Lett.* **43**, 2716–2722 (2016).
33. Camus, P. et al. Statistical wave climate projections for coastal impact assessments. *Earth's Future* **5**, 918–933 (2017).
34. Wang, X. L., Feng, Y. & Swail, V. R. Climate change signal and uncertainty in CMIP5-based projections of global ocean surface wave heights. *J. Geophys. Res. Oceans* **120**, 3859–3871 (2015).
35. Vousdoukas, M. I. et al. Global probabilistic projections of extreme sea levels show intensification of coastal flood hazard. *Nat. Commun.* **9**, 2360 (2018).
36. Vousdoukas, M. I. et al. Climatic and socioeconomic controls of future coastal flood risk in Europe. *Nat. Clim. Change* **8**, 776–780 (2018).
37. Hinkel, J. et al. Coastal flood damage and adaptation costs under 21st century sea-level rise. *Proc. Natl Acad. Sci. USA* **111**, 3292–3297 (2014).
38. Hallegatte, S., Green, C., Nicholls, R. J. & Corfee-Morlot, J. Future flood losses in major coastal cities. *Nat. Clim. Change* **3**, 802–806 (2013).
39. Wahl, T. et al. Understanding extreme sea levels for broad-scale coastal impact and adaptation analysis. *Nat. Commun.* **8**, 16075 (2017).
40. Arkema, K. K. et al. Coastal habitats shield people and property from sea-level rise and storms. *Nat. Clim. Change* **3**, 913–918 (2013).
41. Hemer, M., Wang, X., Webb, A. & COWCLIP contributors *Report of the 2018 Meeting for the WCRP-JCOMM Coordinated Ocean Wave Climate Project (COWCLIP)* (WMO, 2018).
42. Hemer, M., Wang, W., Charles, E., Hegermiller, C. & COWCLIP contributors *Report of the 2014 Meeting for the WCRP-JCOMM Coordinated Global Wave Climate Projections (COWCLIP)* (WMO, 2014).
43. Ribal, A. & Young, I. R. 33 years of globally calibrated wave height and wind speed data based on altimeter observations. *Sci. Data* **6**, 77 (2019).
44. Stopa, J. E. & Cheung, K. F. Intercomparison of wind and wave data from the ECMWF Reanalysis Interim and the NCEP Climate Forecast System Reanalysis. *Ocean Model.* **75**, 65–83 (2014).
45. Dee, D. P. et al. The ERA-Interim reanalysis: configuration and performance of the data assimilation system. *Q. J. R. Meteorol. Soc.* **137**, 553–597 (2011).
46. Taylor, K. E. Summarizing multiple aspects of model performance in a single diagram. *J. Geophys. Res. Atmos.* **106**, 7183–7192 (2001).
47. Wang, X. L., Feng, Y. & Swail, V. R. Changes in global ocean wave heights as projected using multimodel CMIP5 simulations. *Geophys. Res. Lett.* **41**, 1026–1034 (2014).
48. Kar-Man Chang, E. CMIP5 projected change in Northern Hemisphere winter cyclones with associated extreme winds. *J. Clim.* **31**, 6527–6542 (2018).
49. Karnauskas, K. B., Lundquist, J. K. & Zhang, L. Southward shift of the global wind energy resource under high carbon dioxide emissions. *Nat. Geosci.* **11**, 38–43 (2018).
50. Sigmond, M., Reader, M. C., Fyfe, J. C. & Gillett, N. P. Drivers of past and future Southern Ocean change: stratospheric ozone versus greenhouse gas impacts. *Geophys. Res. Lett.* **38**, L12601 (2011).
51. Millar, R. J. et al. Emission budgets and pathways consistent with limiting warming to 1.5 °C. *Nat. Geosci.* **10**, 741–747 (2017).
52. Sierra, J. P. & Casas-Prat, M. Analysis of potential impacts on coastal areas due to changes in wave conditions. *Climatic Change* **124**, 861–876 (2014).
53. Vousdoukas, M. I., Mentaschi, L., Voukouvalas, E., Verlaan, M. & Feyen, L. Extreme sea levels on the rise along Europe's coasts. *Earth's Future* **5**, 304–323 (2017).
54. Sallenger, Jr, A. H., Doran, K. S. & Howd, P. A. Hotspot of accelerated sea-level rise on the Atlantic coast of North America. *Nat. Clim. Change* **2**, 884–888 (2012).
55. Almar, R. et al. Response of the Bight of Benin (Gulf of Guinea, West Africa) coastline to anthropogenic and natural forcing. Part 1: Wave climate variability and impacts on the longshore sediment transport. *Cont. Shelf Res.* **110**, 48–59 (2015).
56. Khon, V. C. et al. Wave heights in the 21st century Arctic Ocean simulated with a regional climate model. *Geophys. Res. Lett.* **41**, 2956–2961 (2014).
57. Jacob, D. et al. EURO-CORDEX: new high-resolution climate change projections for European impact research. *Reg. Environ. Change* **14**, 563–578 (2014).
58. Stopa, J. E. Wind forcing calibration and wave hindcast comparison using multiple reanalysis and merged satellite wind datasets. *Ocean Model.* **127**, 55–69 (2018).
59. Campos, R. M., Alves, J. H. G. M., Guedes Soares, C., Guimaraes, L. G. & Parente, C. E. Extreme wind-wave modeling and analysis in the south Atlantic Ocean. *Ocean Model.* **124**, 75–93 (2018).
60. Hasselmann, S., Hasselmann, K., Allender, J. H. & Barnett, T. P. Computations and parameterizations of the nonlinear energy transfer in a gravity-wave spectrum. Part II: parameterizations of the nonlinear energy transfer for application in wave models. *J. Phys. Oceanogr.* **15**, 1378–1391 (1985).
61. van Vledder, G. P., C. Hulst, S. T. & McConochie, J. D. Source term balance in a severe storm in the Southern North Sea. *Ocean Dynam.* **66**, 1681–1697 (2016).
62. Dietrich, J. C. et al. Limiters for spectral propagation velocities in SWAN. *Ocean Model.* **70**, 85–102 (2013).
63. Reguero, B. G., Losada, I. J. & Méndez, F. J. A recent increase in global wave power as a consequence of oceanic warming. *Nat. Commun.* **10**, 205 (2019).

64. Stammer, D., Van Der Wal, R., Nicholls, J. R. & Schlosser, P. *WCRP/IOC Sea Level 2017 Conference Statement. International WCRP/IOC Conference 2017 – Regional Sea Level Changes and Coastal Impacts* (Columbia Univ., 2017).

Acknowledgements

This study represents Task 3 of the second phase of COWCLIP (<https://cowclip.org/>), an international collaborative working group endorsed by the Joint Technical Commission for Oceanography and Marine Meteorology, a partnership between the World Meteorological Organization and the Intergovernmental Oceanographic Commission of UNESCO. We acknowledge the different climate-modelling groups, the Program for Climate Model Diagnosis and Intercomparison and the World Climate Research Program's Working Group on Coupled Modelling. We acknowledge ECMWF for availability of ERAI data, and Australia's Integrated Marine Observing System for altimeter wind/wave data, used for model validation. J.M., M.H. and C.T. acknowledge the support of the Australian Government National Environmental Science Program Earth Systems and Climate Change Hub. B.T. and M.W. acknowledge the support of the Regional and Global Climate Modeling Program of the US Department of Energy, Office of Science, Office of Biological and Environmental Research, through contract No. DE-AC02-05CH11231, and the National Energy Research Supercomputing Center of the LBNL. I.Y. acknowledges ongoing support from the Australian Research Council through grant No. DP160100738, and to the Integrated Marine Observing System. N.M., T.S., A.B. and B.K. acknowledge the support of the TOUGOU Program by MEXT, Japan, JSPS-Kakenhi Program. L.E. acknowledges the support of the US Geological Survey Coastal and Marine Hazards/Resources Program. Ø.B. and O.A. acknowledge the support of the Research Council of Norway through the ExWaMar project through grant No. 256466. We thank all contributors to the COWCLIP project, including C. Appendini (National Autonomous University of Mexico, Mexico), F. Ardhuij (Ifremer, France), N. Groll (Helmholtz-Zentrum Geesthacht Zentrum, Germany), S. Gallagher (Met Éireann, Ireland), S. Gulev (Moscow State University, Russia) and W. Perrie (Bedford Institute of Oceanography, Canada).

Author contributions

All authors (except C.T., N.C., M.W., B.T. and F.A.) had input into experimental design via workshops. J.M. led the analysis of ensemble, algorithm development for data analysis

and writing of the manuscript. M.H. co-led and conceived the experiment, supervised analysis, provided CSIRO ensemble data and co-wrote the manuscript. X.L.W. co-led and conceived the experiment, developed community codes, provided ECCC ensemble data and contributed to analysis and writing of the manuscript. N.C. supervised analysis and contributed to writing the manuscript. C.T. provided CSIRO ensemble data, coordinated data and contributed to writing the manuscript. I.Y. provided satellite data and contributed to analysis and writing the manuscript. A.S. provided IHE ensemble data and contributed to analysis and writing the manuscript. N.M. and T.S. provided KU ensemble data and contributed to writing the manuscript. L.E. provided USGS ensemble data and contributed to writing the manuscript. O.A. and Ø.B. contributed ERAI statistics. M.D., A.B. and J. Staneva contributed IHE ensemble data. L.M. contributed Joint Research Centre ensemble data and developed community codes. M.C.-P. contributed ECCC ensemble data and contributed to writing the manuscript. P.C. and M.M. contributed IHC ensemble data and contributed to writing the manuscript. B.T. and M.W. contributed LBNL ensemble data and contributed to writing the manuscript. L.B. and J.W. contributed NOC ensemble data. A.W. and B.K. had input via workshops. J. Stopa contributed to analysis and writing the manuscript. F.A. assisted with figure development.

Additional information

Supplementary information is available for this paper at <https://doi.org/10.1038/s41558-019-0542-5>.

Reprints and permissions information is available at www.nature.com/reprints.

Correspondence and requests for materials should be addressed to J.M.

Peer review information: *Nature Climate Change* thanks Gonéri Le Cozannet and the other, anonymous, reviewer(s) for their contribution to the peer review of this work.

Publisher's note: Springer Nature remains neutral with regard to jurisdictional claims in published maps and institutional affiliations.

© The Author(s), under exclusive licence to Springer Nature Limited 2019

Methods

Data contribution. We use a community-derived ensemble compiled from ten CMIP5-based global wind-wave climate projection studies^{25–34}, completed under a pre-designed framework^{41,42}. Annual and seasonal means of significant wave height (H_s), mean wave period (T_m), mean wave direction (θ_m) as well as tenth/ninety-ninth percentiles of annual/seasonal H_s were obtained from the ten individual studies. Consult Supplementary Information for a detailed description of the datasets considered and framework.

Our analysis assesses projected relative changes between the representative current (1979–2004) and future (2081–2100) time-slices. These time periods align with the CMIP5 GCM archives of high-temporal resolution atmospheric fields used to develop wind-wave projections, and correspond to the common period across nine of the ten contributing datasets (see Supplementary Information, Section 1.1 and Supplementary Table 1). Contributed datasets are considered under two different greenhouse-gas RCPs—RCP4.5 and RCP8.5—describing, respectively, medium-stabilizing and high-radiative forcing scenarios reaching +4.5 W m⁻² and +8.5 W m⁻² (relative to pre-industrial (1850) conditions). Sea-ice regions were excluded from the analysis, to support intercomparison between the different contributions.

Skill of GCM-forced wave climate simulations. As previously mentioned, all contributing studies^{25–34} provided assessments of the skill of their GCM-forced global wind-wave simulations to represent the historical wave climate on an independent basis. Here we use two historical wave datasets (a recently compiled dataset of altimeter measurement records and a well-known global wave reanalysis) exclusively as a common point of reference for our model ensemble intercomparison. The two datasets are briefly described below.

Historical satellite altimeter measurements. We compare the GCM-forced wave simulations to the most recent (and complete) database⁴³ of satellite H_s measurements. This database combines 13 radar altimeters that have been calibrated extensively against the National Oceanographic Data Center buoy data, and cross-validated against an independent compiled buoy dataset supplied by the European Centre for Medium-Range Weather Forecasts (ECMWF)^{43,65}. The dataset contains H_s on a 2°-grid resolution (at global scale) over a period of 33 years (1985–2018). After control analysis, we found only partial data for the period 1985–1989 (for which only GEOSAT data are available) and no data for 1991, which limits the data to 1992–2018, providing a common time-slice duration for comparison of 26 years.

In the comparison of GCM-forced global wave simulations with altimeter measurements, the time-slice mismatch is ignored⁶⁶. Since GCM atmospheric forcing (and the spectral wave models) were not subject to any data assimilation, they are considered as being representative of the historical wave climate regardless of the time period⁶⁶. Note that GCM simulations (and their natural internal climate variability and its associated large-scale modes) are not in temporal phase with the satellite database. We assume that any differences between GCMs and altimeter measurements are attributable to model and observation biases and not to the non-stationarity of the wind-wave climate²³.

To allow for intercomparison, the wave parameters obtained from each of the contributions^{25–34} were collocated onto the satellite-database global grid, preserving the original data. Taylor diagrams⁴⁶ were used to compare the skill of the GCM-forced wave simulations to represent the present H_s climate at both the global and regional scale (Supplementary Figs. 1–3 and 4,5, respectively). We clarify that our Taylor diagrams present a spatial pattern correlation of a temporal average (and not a spatio-temporal correlation). In addition to Taylor diagrams, we present global pairwise comparisons maps of the mean and variability H_s biases for a subset from the full ensemble with common GCM-WMM (Supplementary Table 3), allowing us to identify the spatial variation of the biases (Supplementary Figs. 12,13 and 16,17, respectively).

ERA1 wave reanalysis. In addition to the univariate satellite data⁴⁵, we compare model-skill over the current wave climate (1979–2004) by comparing the present-day GCM-forced global wave simulations to wind-wave parameters obtained from the observationally constrained ECMWF ERA1⁴⁵ global wave reanalysis. ERA1 is a consistent spatially and temporally complete dataset⁴⁵ that has been widely used^{1,25,67} and extensively validated⁴⁴, being considered appropriate for multi-year analysis and modelling of long-term processes⁴⁴. The ERA1 database provides 6-h values of H_s , T_m and θ_m on a 1° global resolution, allowing us to compare all wave variables of interest at the global scale. The ERA1 is therefore used as a well-known reference database, allowing us to compare all contributing simulations under the same reference. We note that, despite its relatively good model-skill against buoy and altimetry measurements⁴⁴, ERA1 still exhibits some biases in the H_s upper percentiles (ninety-fifth and above), where it underestimates altimetry measurements of H_s by ~10–15%⁴⁴.

The original 6-h multivariate ERA1 dataset was used to calculate a standard set of statistics as performed for the contributing studies^{25–34} (see Supplementary Information, Section 2). To allow for intercomparison, the surface wave parameters derived from each of the contributing studies^{25–34} were bilinearly interpolated onto the ERA1 grid. Taylor diagrams⁴⁶ were adopted as a representation of the skill of the

GCM-forced wave simulations to reproduce the present multivariate wave climate (H_s , T_m and θ_m) at both the global and regional scale (Supplementary Figs. 6–8 and 9, respectively). The global pairwise comparison maps of mean and variability bias using the ERA1 dataset are presented in Supplementary Figs. 14,15 and 18,19).

Cluster methodology. We applied an agglomerative-hierarchical clustering analysis, with the similarity criterion defined by Ward's ANOVA-based minimum variance algorithm⁶⁸. The clustering method was used without imposing any restrictions on the number and size, or a priori assumptions, of clusters. Initial cluster distances were derived using a multi-dimensional approach where the pairwise Euclidean distance (D) amongst ensemble members is calculated at every grid location rather than spatially averaged, thereby clustering members with high similarity in terms of spatial pattern and magnitude:

$$D_{i,j,k} = \sqrt{\sum_{k=1}^w (x_{i,k} - x_{j,k})^2} \quad (1)$$

where $x_{i,k}$ and $x_{j,k}$ are the magnitudes of the relative projected change in the annual mean significant wave height from GCMs i and j , respectively, at grid point k , with w equal to the number of ocean grid points. Note that, for the clustering of present-day wave simulations, we have used absolute values rather than relative changes. The usage of annual \bar{H}_s as our clustering variable is based on the fact that \bar{H}_s is the only parameter available from all the contributions and that our main objective is to analyse the total community ensemble of wave simulations. Note that statistical method-derived members^{33,34} from ECCC(s) and IHC did not provide wave period and/or directions (Supplementary Table 1). We also carried out a multivariate clustering based on annual \bar{H}_s , \bar{T}_m and $\bar{\theta}_m$ (not shown) using our dynamical subset of simulations, which showed results qualitatively similar to the \bar{H}_s -based clustering in both the present-day simulations and projected relative changes. Further description of the clustering method application to the present-day climate and the projected relative changes is provided below.

Application to present-day simulations. Annual \bar{H}_s from each GCM-forced global wave simulation over the present-day time-slice (1979–2004) was used in the clustering method (equation (1)). We included all existing ensemble models as well as the mean of each individual contributing study ensemble, a uniformly weighted ensemble mean (that is, attributing equal weight to individual members) and an ensemble mean weighted by WMM. The latter consisted of reducing the full ensemble to n members with each single member representing the mean from a specific WMM (when suitable). For example, the 30-model IHC ensemble was reduced to one member, representing its ensemble mean. The relative differences (%) between the average of all members within each main cluster and the satellite data were calculated separately for each parameter, simply to highlight the key qualities of each cluster (Fig. 1 and Supplementary Fig. 10). The relative difference was also calculated using ERA1 (Supplementary Fig. 11). Note that the clustering analysis (Fig. 1) is fully independent from the comparison with the satellite or the ERA1 datasets as described above.

We applied the clustering analysis to annual and seasonal \bar{H}_s values combined, and the results are consistent with those obtained using annual mean values. We also applied the clustering procedure to the other wave parameters (individually) and obtained consistent findings. In all cases, the present-day simulations are strongly dependent on the WMM adopted by each study group to develop future wave fields, as shown in Fig. 1.

Application to projected future changes. To identify and resolve similarities in the projected future change, the clustering procedure (equation (1)) was applied to the projected relative changes in annual \bar{H}_s between the present-day (1979–2004) and future (2081–2100) time-slices, as estimated by each of the GCM-forced global wave simulations:

$$\Delta H_{j,k} = \frac{\bar{H}_{j,k}^{\text{Future}} - \bar{H}_{j,k}^{\text{Present-day}}}{\bar{H}_{j,k}^{\text{Present-day}}} \quad (2)$$

where $\Delta H_{j,k}$ is the projected change by GCM j at each grid node k .

To resolve the relative importance of the three different sources of uncertainty (that is, RCP scenarios, GCMs and WMMs), we use a subset from the full community ensemble where each member shares common GCM-forcing with at least two other members obtained from different WMMs (see Supplementary Table 2). In the clustering of projected relative changes (equation (1)), we also included the mean of each study contribution, the uniformly weighted ensemble mean (see above), the ensemble mean weighted by GCM (see below) and the ensemble mean weighted by WMM (for each RCP). Five key clusters were identified based on the clustering results as an indication of ensemble members with considerable dissimilarity in the projected change values. The mean of all members within each main cluster (when available) was calculated for each wave parameter (Fig. 1 and Supplementary Fig. 25), providing a robust indication of spatial and magnitude dissimilarities over the global ocean.

For completeness, we also applied cluster analysis to the entire community ensemble of global wind-wave projections, yielding consistent dissimilarities and respective associations between all available wave simulations (albeit less clear owing to the large size of the ensemble) (Supplementary Fig. 26).

ANOVA methodology. *Approach and selection of subsets.* Uncertainty in the projected future wave climate changes (2081–2100 relative to 1979–2004) within our community-based, multi-member ensemble arises from three different sources: choice of RCPs, GCMs and WMMs. The latter refers to the different statistical and dynamical wave modelling approaches used to simulate global wind-wave fields (representing different configurations of statistical methods such as transfer functions, training datasets and/or predictor corrections, and/or dynamical wave models including the source-term packages, sea-ice forcing and numerical model resolution). In contrast with other climatic variables (for example, temperature or precipitation), dynamically derived ensembles of wave projections are typically available only for 20-year periods, constrained by the availability GCM-simulated atmospheric surface winds with sufficiently high temporal resolution^{21,42} (Supplementary Table 2). This constrains the testing of projection uncertainty against the natural (temporal) variability.

Hence, we decompose the total ensemble uncertainty in the projected changes in the long-term (20-year) mean of annual/seasonal \bar{H}_s into contributions from the different sources of uncertainty (RCPs, GCMs and WMMs) and the interactions among them. The fraction of uncertainty attributable to each source (at each grid node) is determined using a three-factor ANOVA⁶⁹-based variance partition method (see below). The method was applied separately to three opportunity subsets obtained from the full ensemble, with each subset containing all three sources of uncertainty (Supplementary Table 3). No other subsets with the same number of factors exist in this community ensemble. Note that the forcing GCMs within subsets 2 and 3 represent a broad cross-section of the CMIP5 ensemble¹⁹, particularly that with availability of high-temporal resolution surface wind fields, in terms of model components⁷⁰ and various GCM characteristics such as spatial resolution⁷⁰.

Subsampling scheme. The ANOVA-based variance decomposition using different sample sizes of variance sources results in biased variance estimators⁷¹ (Fig. 4 and Supplementary Figs. 27–29). To reduce such biases in estimates of variance for quantification of the uncertainty contribution, we complemented the ANOVA-based variance decomposition with a subsampling methodology previously proposed⁷¹. In each subsampling iteration i , we selected two each from n climate models and m wave models, representing a total of $C_2^n C_2^m$ subsamples, with n and m denoting the number of GCMs and WMMs within each subset, respectively. For each subsample iteration i , we end up with two GCMs, two RCPs and two WWM approaches, which we used for variance decomposition as described below.

Three-factor ANOVA model-based variance decomposition. Letting Y_{jkl}^i be our response variable, representing the projected change in \bar{H}_s from the j th GCM, k th RCP and l th WMM, we define our three-factor ANOVA-based partition model⁷¹ without replication following refs. ^{71,72}:

$$Y_{jkl}^i = \mu^i + \alpha_j^i + \beta_k^i + \gamma_l^i + (\alpha\beta)_j^i + (\alpha\gamma)_{jl}^i + (\beta\gamma)_{kl}^i + \delta_{jkl}^i \quad (3)$$

where μ^i is the grand-mean projected change of subsample i . The terms α_j^i , β_k^i and γ_l^i represent the variance arising solely from factors GCMs, WMMs and RCPs (respectively), with j , k and l denoting samples of the different factors ($j=1, 2$, $k=1, 2$ and $l=1, 2$) for each subset of simulations by a combination of two GCMs and two WMMs for two RCPs. The terms $(\alpha\beta)_j^i$, $(\alpha\gamma)_{jl}^i$ and $(\beta\gamma)_{kl}^i$ represent the interactions between the specified pair of factors (that is, two-factor interaction terms). The term δ_{jkl}^i represents the variance arising from the three-factor interactions $(\alpha\beta\gamma)_{jkl}^i$ and internal variability. Note that here the natural internal variability is negligible, as we are analysing differences between two climatological mean values—that is, involving very little temporal variance. Because there are no replications for estimating internal variability, we cannot—and did not—test the statistical significance of variance arising solely from each factor against the natural variability, and thus did not require any assumptions for the residuals of model. The results derived from each subsample i are the unbiased estimates of fraction of the total uncertainty attributable to each source^{71,73}, with the variance fraction η^2 for each factor derived as

$$\eta_{\text{GCM}}^2 = \frac{1}{I} \sum_{i=1}^I \frac{\text{SS}_{\alpha_i^i}}{\text{SS}_{T_i}} \quad (4)$$

$$\eta_{\text{WMM}}^2 = \frac{1}{I} \sum_{i=1}^I \frac{\text{SS}_{\beta_i^i}}{\text{SS}_{T_i}} \quad (5)$$

$$\eta_{\text{RCP}}^2 = \frac{1}{I} \sum_{i=1}^I \frac{\text{SS}_{\gamma_i^i}}{\text{SS}_{T_i}} \quad (6)$$

$$\eta_{\text{GCM-WMM}}^2 = \frac{1}{I} \sum_{i=1}^I \frac{\text{SS}_{\alpha\beta_i^i}}{\text{SS}_{T_i}} \quad (7)$$

$$\eta_{\text{GCM-RCP}}^2 = \frac{1}{I} \sum_{i=1}^I \frac{\text{SS}_{\alpha\gamma_i^i}}{\text{SS}_{T_i}} \quad (8)$$

$$\eta_{\text{RCP-WMM}}^2 = \frac{1}{I} \sum_{i=1}^I \frac{\text{SS}_{\beta\gamma_i^i}}{\text{SS}_{T_i}} \quad (9)$$

$$\eta_{\text{RCP-GCM-WMM}}^2 = \frac{1}{I} \sum_{i=1}^I \frac{\text{SS}_{\delta_i^i}}{\text{SS}_{T_i}} \quad (10)$$

where SS represents sums of squares in each respective factor sample and total. Values of 0 and 1 for the variance fraction η_x^2 correspond to 0 and 100% contribution of factor x to the total ensemble variance (uncertainty), respectively. The average variance fractions are presented in Fig. 5 for each factor and for the sum of all the interaction terms, to compare the relative magnitude of each source of uncertainty. An assessment of the significance of the projected changes relative to the magnitude of natural internal variability is provided in Supplementary Fig. 20, based on one realization available for each member (Supplementary Table 1).

Analysis of projected change. Projected changes in all wave variables (except $\bar{\theta}_m$) between the present and future time-slices were calculated as percentage changes, for each member (from each contribution), directly forced by GCM-simulated surface wind or pressure fields. The Lawrence Berkeley National Laboratory (LBNL)³¹ and Kyoto University³² data were derived using down-scaled forcing via high-resolution atmospheric models driven by particular sea surface temperature conditions (Supplementary Information, Section 1.1), and therefore were not included in this analysis.

Projected changes in $\bar{\theta}_m$ were calculated as absolute values and are shown as clockwise (anticlockwise) rotation in degrees relative to the present-day climate mean. Projected changes were calculated under RCP4.5/8.5. A weighted multi-member ensemble mean of projected changes was then calculated. Fifty statistical wave projections are available from IHC and ECCC(s) combined (for both scenarios), whilst the dynamical projections consist of 23 (RCP4.5) and 25 (RCP8.5) projected change scenarios, as per Supplementary Table 1. Because the projected relative change is strongly dependent on GCM-forcing (atmospheric wind or pressure fields from which the wave field originates) (Figs. 4,5), a weighted multi-member ensemble mean was calculated by applying a weighting factor to each member:

$$\bar{x}_k = \frac{\sum_{i=1}^n (\Delta_{i,k} \times W_{i,k})}{\sum_{i=1}^n (W_{i,k})} \quad (11)$$

where $\Delta_{i,k}$ is the projected change for a given wave parameter k by the ensemble member i , and W_i is the weighting factor for ensemble member i for that same parameter (determined as the number of ensemble members with that same forcing GCM amongst all members, n). For all wave parameters, the global map of mean projected change was derived as the n -member ensemble weighted mean difference between projected and present wave climate fields from equation (11).

Robustness measure. We use a methodology¹⁸ identified by the IPCC AR5 WG1 (ref. ⁷⁴) as being a suitable, effective method to identify regions of robustness. In contrast to other criteria, this robustness criterion¹⁸ does not ignore the existence of internal climate variability and clearly identifies regions with a lack of member agreement and/or lack of climate signal (by assessing the level of consensus on the significance of change as well as the signal of change)^{18,75}.

We assessed the significance of change projected by each of the ensemble members individually, with a two-tailed Welch's t -test that allows for different variances between present and future time-slices. The test was conducted at the 5% significance level. To define areas of robust projected changes, we first identified areas (grid points) where 50% or more of the ensemble members projected a significant change. Within these areas, we further identified those areas where 90% or more of the ensemble members exhibiting a significant change agreed on the sign of the projected changes—these are the areas of robust changes projected by the ensemble, and are hatched in Fig. 2. Note that we employed a higher threshold (90%) than the default 80%^{18,75} for members' agreement on the sign of the projected changes. The key conclusions are similar when other IPCC-referenced methods were used to measure robustness⁷⁴.

As a complement to the robustness criteria¹⁸, we further confirmed that, within all regions with robust projected changes, the ensemble mean of projected changes is statistically significantly different from zero (that is, it stands out of the intermember variability) according to the result of a one-sample Student's t -test at the 5% significance level.

Percentage of coastline with robust changes in offshore forcing wave conditions. In this analysis, we consider all the available offshore deepwater (≥ 200 m) grid points, distributed along the global coast every ~ 100 km. The coast is taken from the Global Self-consistent Hierarchical High-resolution Geography database⁷⁶. We limit our analysis to offshore changes, owing to the limited ability of the CMIP5 GCMs to adequately capture fetch-limited, near-coastal wind fields and land-sea interactions (for example, orographic and katabatic effects) given their coarse spatial resolution. Nevertheless, we note that our GCM-forced wave simulations exhibit good agreement against near-coast buoys^{30,53}, even within semi-enclosed seas (for example, the Mediterranean)⁵³ and under extreme wave conditions⁷⁷. The model-skill reported for near-coast buoys is comparable to that against offshore buoys and to high-resolution coastal wave hindcasts⁷⁸. Sections of coast without available wave model outputs were not considered, including sea-ice and enclosed seas.

Data availability

The data that support the findings of this study are available from the corresponding author on request, or via the COWCLIP data access portal at <https://cowclip.org/data-access/>.

References

65. Young, I. R., Sanina, E. & Babanin, A. V. Calibration and cross validation of a global wind and wave database of altimeter, radiometer, and scatterometer measurements. *J. Atmos. Ocean. Technol.* **34**, 1285–1306 (2017).
66. Semedo, A. et al. Projection of global wave climate change toward the end of the twenty-first century. *J. Clim.* **26**, 8269–8288 (2013).
67. Kumar, P., Min, S.-K., Weller, E., Lee, H. & Wang, X. L. Influence of climate variability on extreme ocean surface wave heights assessed from ERA-Interim and ERA-20C. *J. Clim.* **29**, 4031–4046 (2016).
68. Ward, J. H. Hierarchical grouping to optimize an objective function. *J. Am. Stat. Assoc.* **58**, 236–244 (1963).
69. Storch, H. V. & Zwiers, F. W. *Statistical Analysis in Climate Research* (Cambridge Univ. Press, 1999).
70. Flato, G. et al. in *Climate Change 2013: The Physical Science Basis* (eds Stocker, T. F. et al.) 741–882 (IPCC, Cambridge Univ. Press, 2013).
71. Bosshard, T. et al. Quantifying uncertainty sources in an ensemble of hydrological climate-impact projections. *Water Resour. Res.* **49**, 1523–1536 (2013).
72. Garcia, R. A., Burgess, N. D., Cabeza, M., Rahbek, C. & Araújo, M. B. Exploring consensus in 21st century projections of climatically suitable areas for African vertebrates. *Glob. Change Biol.* **18**, 1253–1269 (2012).
73. Zhao, Y. et al. Potential escalation of heat-related working costs with climate and socioeconomic changes in China. *Proc. Natl Acad. Sci. USA* **113**, 4640 (2016).
74. Collins, M. et al. in *Climate Change 2013: The Physical Science Basis* (eds Stocker, T. F. et al.) 1041–1042 (IPCC, Cambridge Univ. Press, 2013).
75. Skinner, C. B. & Diffenbaugh, N. S. Projected changes in African easterly wave intensity and track in response to greenhouse forcing. *Proc. Natl Acad. Sci. USA* **111**, 6882 (2014).
76. Wessel, P. & Smith, W. H. F. A global, self-consistent, hierarchical, high-resolution shoreline database. *J. Geophys. Res. Solid Earth* **101**, 8741–8743 (1996).
77. Shope, J. B., Storlazzi, C. D., Erikson, L. H. & Heegermiller, C. A. Changes to extreme wave climates of islands within the Western Tropical Pacific throughout the 21st century under RCP 4.5 and RCP 8.5, with implications for island vulnerability and sustainability. *Glob. Planet. Change* **141**, 25–38 (2016).
78. Perez, J., Menendez, M. & Losada, I. J. GOW2: a global wave hindcast for coastal applications. *Coast. Eng.* **124**, 1–11 (2017).